The Astronomical Journal, 159:155 (14pp), 2020 April https://doi.org/10.3847/1538-3881/ab7454

An Analysis of the Statistics and Systematics of Limb Anomaly Detections in *HST*/STIS Transit Images of Europa

Gabriel Giono[1], Lorenz Roth[1], Nickolay Ivchenko[1], Joachim Saur[2], Kurt Retherford[3], Stephan Schlegel[2], Marcus Ackland[1], and Darrell Strobel[4]
[1] KTH Royal Institute of Technology, Space and Plasma Physics, Teknikringen 31, Stockholm, Sweden; ggiono@kth.se
[2] University of Cologne, Cologne, Germany
[3] Southwest Research Institute, San Antonio, TX, USA
[4] Johns Hopkins University, Baltimore, MD, USA
Received 2019 October 10; revised 2020 February 5; accepted 2020 February 8; published 2020 March 13

Abstract

Several recent studies derived the existence of plumes on Jupiter's moon Europa. The only technique that provided multiple detections is the far-ultraviolet imaging observations of Europa in transit of Jupiter taken by the Space Telescope Imaging Spectrograph (STIS) on the *Hubble Space Telescope* (*HST*). In this study, we reanalyze the three *HST*/STIS transit images in which Sparks et al. identified limb anomalies as evidence for Europa's plume activity. After reproducing the results of Sparks et al., we find that positive outliers are similarly present in the images as the negative outliers that were attributed to plume absorption. A physical explanation for the positive outliers is missing. We then investigate the systematic uncertainties and statistics in the images and identify two factors that are crucial when searching for anomalies around the limb. One factor is the alignment between the actual and assumed locations of Europa on the detector. A misalignment introduces distorted statistics, most strongly affecting the limb above the darker trailing hemisphere where the plumes were detected. The second factor is a discrepancy between the observation and the model used for comparison, adding uncertainty in the statistics. When accounting for these two factors, the limb minima (and maxima) are consistent with random statistical occurrence in a sample size given by the number of pixels in the analyzed limb region. The plume candidate features in the three analyzed images can be explained by purely statistical fluctuations and do not provide evidence for absorption by plumes.

Unified Astronomy Thesaurus concepts: Hubble Space Telescope (761); Ultraviolet photometry (1740); Astrostatistics techniques (1886); Galilean satellites (627)

1. Introduction

The ice crust of Jupiter's moon Europa is relatively young and reveals a variety of features that indicate past geological activity (e.g., Pappalardo et al. 1998; Greeley et al. 2004; Schmidt et al. 2011). Below the ice, there is a global ocean of saline liquid water, detected through magnetic induction signals measured by the *Galileo* spacecraft during several flybys at Europa (Khurana et al. 1998; Zimmer et al. 2000). The presence of some form of outgassing or cryovolcanism has long been speculated and searched for (e.g., Cook et al. 1981; Squyres et al. 1983; Saur et al. 2011), but imaging by the *Galileo* spacecraft, although limited, did not provide any evidence for present-day geophysical activity at Europa (Phillips et al. 2000).

While at Europa, observational evidence for outgassing remained elusive for decades, the *Cassini* spacecraft discovered continuous cryovolcanic activity near the south pole of Saturn's moon Enceladus (Hansen et al. 2006; Porco et al. 2006). The activity at Enceladus leads to the formation of a torus of water-based neutral gas near the small moon's orbit (Shemansky et al. 1993; Johnson et al. 2006). The south polar plumes of Enceladus are also the source for Saturn's E ring (Spahn et al. 2006). The neutral torus detected near Europa's orbit (Lagg et al. 2003; Mauk et al. 2003), in contrast, can be supplied by loss from Europa's global sputtering-generated atmosphere alone, and additional sources like plumes are not required (Smyth & Marconi 2006).

In 2012 December, far-ultraviolet (FUV) spectral imaging of Europa by the Space Telescope Imaging Spectrograph (STIS) of the *Hubble Space Telescope* (*HST*) revealed localized emission surpluses at both the hydrogen Lyα line and the oxygen 1304 Å multiplet. These emissions were shown to be consistent with a transient H_2O abundance in a small region above the southern anti-Jovian hemisphere, possibly sourced by active H_2O outgassing (Roth et al. 2014b). Follow-up spectral imaging did not reveal a similar signal in images taken between 2014 and 2016 (Roth et al. 2014a, 2016).

Also using *HST*/STIS, Sparks et al. (2016) imaged Europa while the moon transited Jupiter, searching for signs of active plumes. The authors reported the detection of absorption patches above Europa's limb in three images in Sparks et al. (2016) and a repeated detection of one of the patches in follow-up observations (Sparks et al. 2017). The data do not allow determination of the absorbing species, but the patches were interpreted as originating from continuous absorption by H_2O gas and related to outgassing similar to the phenomenon from the study of Roth et al. (2014b). The features detected in the transit images are located on the trailing southern hemisphere and require an H_2O column density about 1 order of magnitude larger than that derived from the spectral emissions in Roth et al. (2014b).

A search with the Near-InfraRed SPECtrograph (NIRSPEC) of the Keck Observatory in 2016 and 2017 provided the first direct detection of water vapor at Europa on one date, as well as nondetections on 16 other dates (Paganini et al. 2020). The singular detection and derived water vapor abundance are

consistent with sporadic plume outgassing as a source. The water vapor signal was measured over the anti-Jovian/trailing quadrant, near the longitude of the Roth et al. (2014b) detection but roughly opposite the longitudes of the features detected by Sparks et al. (2016, 2017).

Additional evidence for atmospheric inhomogeneity was found in archived in situ data taken during flybys of the *Galileo* spacecraft at Europa. Magnetic field perturbations during flyby E26 were first tentatively related to plumes by Blöcker et al. (2016) through comparisons with magnetohydrodynamic model results. Using a hybrid model, Arnold et al. (2020) then more confidently related one signal measured during E26 to an active plume. Jia et al. (2018) also showed that a short perturbation in the magnetic field data and a simultaneous spike in the upper hybrid frequency are consistent with the presence of narrow neutral density enhancement near the closest approach of the *Galileo* flyby E12 at Europa. There is some agreement in the shape of the plumes assumed to interpret the *Galileo* data, but there are differences in location, density, and distribution of the neutral gas. The E12 and E26 flybys were the ones with the closest approaches to Europa (C/A closer than 400 km) and are thus particularly well suited to search for plumes.

Finally, McGrath & Sparks (2017) pointed out that the maximum electron density near Europa coincides roughly with one of the locations from Sparks et al. (2016). However, the slightly eastward located plume in Jia et al. (2018) is collocated with a minimum in detected electron density from *Galileo*, as also noted in Sparks et al. (2019).

Taken together, there is a set of recent studies deriving evidence for active cryovolcanic outgassing. The derived plume characteristics are not consistent in a way that they can all be explained by the same localized geyser that frequently erupts in a similar way. Instead, the studies suggest various forms of outgassing (as far as the plumes can be characterized with the data) at various locations. Despite these apparent differences in location and abundance, all the detections of plume-related features are generally seen to support each other in the case that active outgassing is present at Europa (e.g., Grasset et al. 2017; Jia et al. 2018; Smith et al. 2019; Arnold et al. 2020).

Cassini UVIS spectra of the plumes of the Saturnian moon Enceladus when observed in transit of Saturn revealed that absorption at the FUV wavelengths of the Sparks et al. (2016) images is not detectable (Hansen et al. 2019). However, the Enceladus plumes were marginally detectable during the same Saturn transit at the Lyα line (1216 Å). The detection at Lyα and nondetection at longer FUV wavelengths of the Enceladus plumes can be explained by the higher-absorption cross section at Lyα (Yoshino et al. 1996; Mota et al. 2005).

In the case of Europa, the frequency of detections and nondetections at different wavelengths and with different methods is yet puzzling. Sparks et al. (2017) stated that in about 17% of the FUV transit images, plumes are observed, and at these wavelengths, a column density of about 10^{17} cm^{-2} is required for a detection for the water vapor cross section (Mota et al. 2005; Hansen et al. 2019). Spectral *HST*/STIS observations of Europa also in transit of Jupiter by Roth et al. (2017) were used to look for absorption at Lyα similar to Enceladus (Hansen et al. 2019). However, plume signatures were not detected on six occasions, despite a slightly higher sensitivity at a lower spatial resolution. Moreover, the method used for the initial detection by Roth et al. (2014b) requires an estimated column density of only 10^{16} cm^{-2} for detectable Lyα emission, but no plume signals were detected in two earlier or 17 follow-up (after first detection) observations by *HST*/STIS emission observations. The Keck NIRSPEC observations by Paganini et al. (2020) reach a slightly higher sensitivity but only lead to one marginally significant detection out of 17 attempts. Hence, there appears to be a discrepancy between the detection rate and sensitivity of the different observing methods, with the nominally less sensitive method providing more detections of a putatively similar plume phenomenon.

In order to independently evaluate the sensitivity of the FUV transit observations, we reanalyze the three *HST*/STIS images reported to provide plume features by Sparks et al. (2016). The aim is to provide independent results of this plume evidence, as well as to systematically investigate the dependencies of the statistical results on the model assumptions. Section 2 shows similar results reproduced using the methodology described in their article. However, this analysis reveals the presence of positive outliers with similar significance as the negative outliers interpreted as plume signatures, as well as some important sources of uncertainty pertaining to the positioning of Europa's center with respect to the model and the modeling of Europa disk reflectance that have not been quantitatively addressed in Sparks et al. (2016). Section 3 discusses the implication of these uncertainties and their influence on the detection level of the plume candidates.

2. Reproducing Results from Sparks et al. (2016)

In this section, we describe the reproduction of the results presented by Sparks et al. (2016). The methodology described in their article was followed as closely as possible. We describe most of the steps in our own words and point out where our analysis differs from the analysis in Sparks et al. (2016). For more details on the original analysis, the reader is referred to the original article by Sparks et al. (2016).

2.1. Data Processing

The three *HST*/STIS Europa transit observations reported to reveal plume candidates by Sparks et al. (2016) were selected for this study. The exposures taken on 2014 January 26 at 18:05, 2014 February 27 at 19:57, and 2014 April 4 at 5:20, respectively, have root IDs oc7u02g2q, ochz03dwq, and ochz05ftq in the *HST* data archive. The observations were carried out using the STIS (Proffitt et al. 2010) and the FUV filter F25SRF2. In all of the transit observations of Sparks et al. (2016), the pointing of the telescope was deliberately set such that Europa is moving across the STIS detector in order to allow for separating detector artifacts from anomalies in the (moving) Europa frame. This approach by Sparks et al. (2016) sets the primary *HST* tracking centered on Europa with a superimposed artificial moving target "Level 3" drift. As a first step, the image therefore had to be reconstructed in the comoving reference frame using the corresponding jitter file and ephemeris of *HST*.

The detector counts were mapped onto a fixed 35 km pixel^{-1} frame instead of the native pixel resolution of the detector in order to obtain the same apparent radius of Europa for all three observations, as the pixel scale in the different observations changed depending on the distance between Earth and Jupiter. Each count was giving a $1/f$ weight, where f

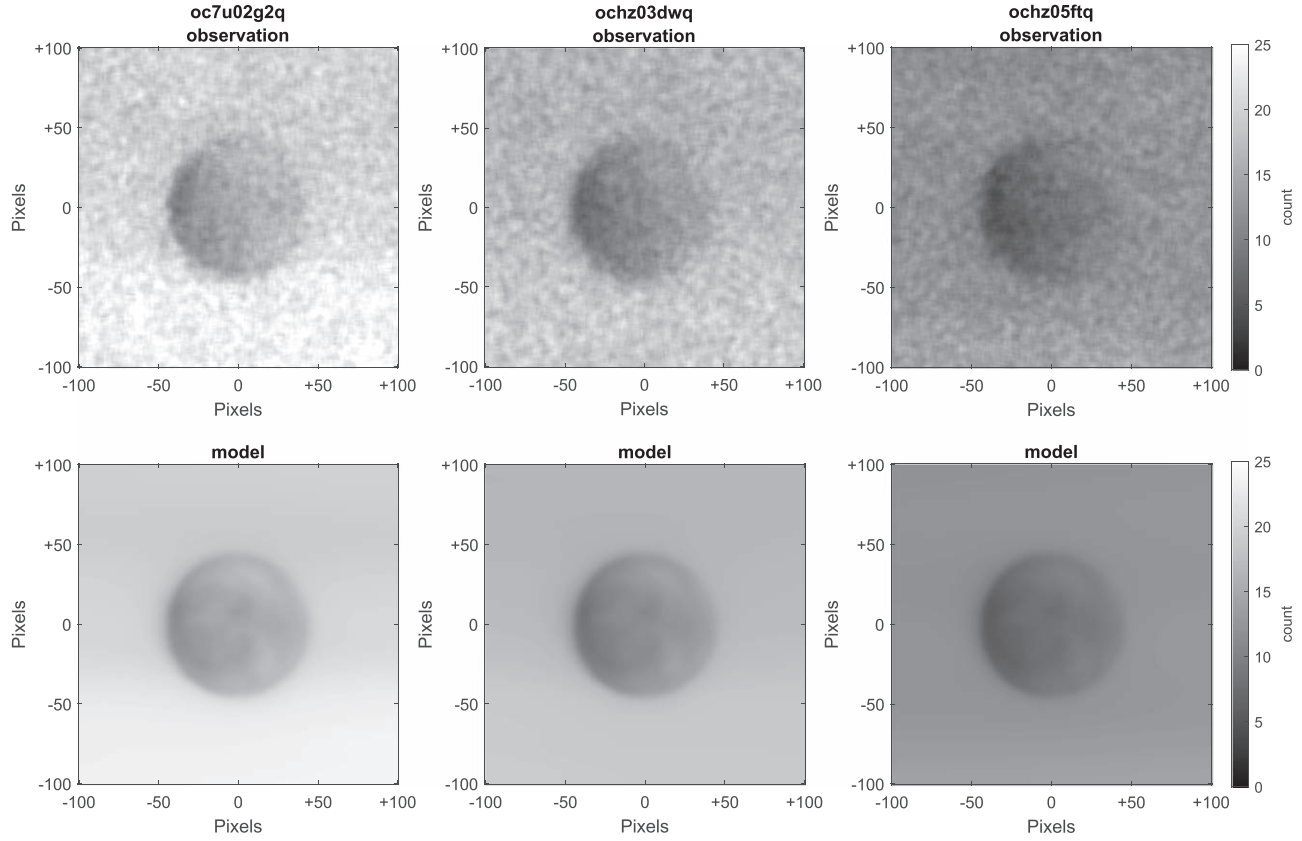

Figure 1. Observation (top row) and corresponding model (bottom row) for oc7u02g2q (left), ochz03dwq (middle), and ochz05ftq (right) in the 35 km pixel^{-1} frame, after the 5 × 5 moving average filter.

is the value of the flat field for the corresponding pixel on the detector, effectively taking into account the detector flat field. The Europa north direction was also rotated to the top of the frame using ephemeris information retrieved from SPICE. The sky brightness was determined based on the average photon count at a dark corner of the observation (i.e., away from the Jupiter background) in a 200 by 200 pixel region and removed from the entire image. The spatially averaged sky brightness was 0.10, 0.46, and 0.73 counts for oc7u02g2q, ochz03dwq, and ochz05ftq, respectively, with a corresponding 1σ uncertainty of 0.09, 0.23, and 0.23 calculated as the standard deviation inside the region. The processed observations are shown in the top row of Figure 1, which corresponds to Figure 4 in Sparks et al. (2016).

2.2. Modeling the Observation

The observations were modeled by combining an estimation of Jupiter's background brightness with a model of Europa's reflectance. For generating the Jovian background image, we chose a slightly different approach compared to the approach of Sparks et al. (2016), in which they estimated the background by masking the location of Europa with a disk of radius $1.2R_E$ during the reconstruction of the image. Since both Europa and the Jupiter clouds move during the exposure, an estimation of the signal from the Jovian background behind Europa can be retrieved. However, the estimation of the background close to the disk is limited, as the region around Europa is masked during part of the exposure, possibly resulting in lower counts in the background region around the limb. The approach we took for the background image was to get a linear fit along each row of the Europa-frame image, excluding the central part where Europa is located. This is based on the assumption that the band structures seen in the atmosphere of Jupiter are smooth and lie horizontally in the Europa north-up reference frame of the observation. The resulting background image was then smoothed vertically (16 pixels moving average) to reduce discontinuities between the rows. Although Sparks et al. (2016) used a different method, they also mentioned that all horizontal variations in their background image are smooth.

For the spatial structure of the reflectance of Europa's surface, we followed the analysis of Sparks et al. (2016). Their modeling assumes a linear scaling of the visible albedo to the UV albedo, which was taken from the *Galileo* survey observations, adjusting the contrast of the disk albedo with a contrast parameter C, taken as 1.61. Mathematically, this can be expressed as

$$A_{\mathrm{UV}} = C \times (A_{\mathrm{visible}} - \langle A_{\mathrm{visible}} \rangle) + \langle A_{\mathrm{visible}} \rangle, \quad (1)$$

where A_{visible} is the disk albedo at visible wavelengths taken from the *Galileo* survey and A_{UV} is the UV albedo.

The reflectance of the disk is then obtained by multiplying the UV albedo with the disk Oren–Nayar reflectance (Oren & Nayar 1994), calculated with a roughness parameter $\sigma_{\mathrm{Oren-Nayar}}$ of 0.57 as stated in Sparks et al. (2016). This parameter is linked to the standard deviation of the surface roughness. This is expressed as

$$R_{\mathrm{disk}} = A_{\mathrm{UV}} \times R_{\mathrm{Oren-Nayar}}, \quad (2)$$

where R_{disk} is the reflectance of the disk and $R_{\mathrm{Oren-Nayar}}$ is the Oren–Nayar reflectance.

The disk brightness is computed by scaling the disk reflectance by the observed average brightness of Europa's disk,

$$B_{\text{disk}} = (R_{\text{disk}} / \langle R_{\text{disk}} \rangle) \times \langle B_{\text{observation}} \rangle, \quad (3)$$

where B_{disk} is the disk brightness and $B_{\text{observation}}$ is the observation disk brightness.

The final model of brightness M is obtained by adding the modeled brightnesses of the background Jupiter surface $B_{\text{background}}$ (outside the Europa disk, i.e., $B_{\text{background}} = 0$ for $r < R_E$) and the Europa disk (inside the disk, i.e., $B_{\text{disk}} = 0$ for $r > R_E$) multiplied by a scaling factor s_D and then convolving it with the Tiny Tim point-spread function (PSF) of *HST*, rotated to the Europa north-up orientation:

$$M = \text{PSF} * (s_D \times B_{\text{disk}} + B_{\text{background}}). \quad (4)$$

Figure 1 shows the three *HST*/STIS observations with their corresponding model M.

The introduction of the scaling factor s_D was motivated by the fact that the average on-disk residual had been offset from zero. The offset from zero is introduced by the convolution with the PSF, as background signal propagates onto the disk. This can be corrected for by multiplying the disk model with a scaling factor prior to the convolution, as was performed in Roth et al. (2017). The correction factor s_D was 0.90, 0.89, and 0.88 for oc7u02g2q, ochz03dwq, and ochz05ftq, respectively. Note that this correction was not mentioned by Sparks et al. (2016), but not including it resulted in a visually quite different residual when dividing the observation by the model compared to the ones shown in Sparks et al. (2016; e.g., left of Figure 5 in their article). We therefore assumed a similar correction was applied by Sparks et al. (2016) and decided to include it.

2.3. Statistics of Observation versus Model Comparison: Z- and P-statistic Results

The photon count of the observation is referred to hereafter as I_{obs}, whereas the model photon count is I_0, following Sparks et al.'s (2016) notation. A 5×5 moving average filter ("boxcar") was applied to both the observation and the model to increase the signal-to-noise ratio. This is achieved by convolving them with a 5×5 kernel with values $1/25$. It is worth pointing out that using a Gaussian filter (or an Epanechnikov filter) is less biased compared to a simple average filter (Silverman 1986). However, the latter was used for the sake of reproducing Sparks et al.'s (2016) analysis. The resulting averaged observation and model are respectively denoted as $\langle I_{\text{obs}} \rangle_{5\times5}$ and $\langle I_0 \rangle_{5\times5}$. The ratio between observation and model $\langle I_{\text{obs}} \rangle_{5\times5} / \langle I_0 \rangle_{5\times5}$ was then computed. Note that the order of the averaging is different from Sparks et al. (2016), where the averaging is done after dividing with the model, i.e., $\langle I_{\text{obs}} / I_0 \rangle_{5\times5}$. If the goal is to increase the signal-to-noise ratio in the image, the moving average filtering should be applied before the division and not after, as the operation is not linear. Sparks et al. (2016) argued that doing so would lead to a luminosity-weighted optical depth that could bias the measurements to low values of τ, with the optical depth τ being defined as $\langle \tau \rangle = 1 - \langle I_{\text{obs}} / I_0 \rangle$. However, both approaches were tested, and we observed the opposite: averaging after taking the ratio increased the significance of the statistical outliers with lower τ (i.e., negative outliers in the z statistic, described in a later paragraph) by about 2% compared to averaging before taking the ratio. Nevertheless, the difference between both approaches is negligible. Since averaging before taking the ratio is more logical for increasing the signal-to-noise ratio, we decided to use this approach.

Locating Europa in the observation image is another crucial detail: positional uncertainty between the observation and the model introduces errors, particularly at the limb, when computing their ratio. The absolute position of the center of Europa in the frame is unknown due to the uncertainty of the absolute pointing of *HST* (Proffitt et al. 2010). Sparks et al. (2016) considered manual adjustment of the disk position, and, for the purpose of this section, a manual shift of the observation with respect to the model providing the best agreement with the results from Sparks et al. (2016) is used.

The z statistic is obtained as $z = (\langle I_{\text{obs}} \rangle_{5\times5} / \langle I_0 \rangle_{5\times5} - 1)/\sigma$. This is a standard $z$test also used in Sparks et al. (2016), where z is constructed as a normal distribution characterizing the difference between the observation and the model. The z-statistic distribution is normalized by σ, which corresponds to the uncertainty in the observation. Sparks et al. (2016) derived σ for each pixel of their model assuming the noise of the observation is purely Poisson noise, using the formula $\sigma(\langle I_{\text{obs}} / I_0 \rangle) = \frac{1}{n}\sqrt{\langle 1/I_0 \rangle + S \langle 1/I_0 \rangle^2}$ (where $n = 5$ for a 5×5 averaging and S is the average sky brightness count). They tested this in the background, taking samples in an annulus from 2 to 4 Europa radii, indeed showing that the distribution of the z statistic is normalized (i.e., $\sigma_z = 1$) in the background. However, this method requires the model to perfectly match the observation brightness. This appears to work for the background in the Sparks et al. (2016) case, as it was obtained from the observation itself, but does not hold for the on-disk illumination, as well as the region outside the limb due to the PSF smearing and the possibly lower count rate due to the background reconstruction. In these regions (on-disk and limb), the model might not match the observation adequately. This mismatch between observation and model would introduce an additional source of error for z on each pixel, making the resulting total error larger than purely Poisson noise and therefore leading to a slightly skewed z-statistic distribution. The effect of model mismatch on the z statistic is an important issue, and it will be referred to in the rest of the article. A simple example showing this effect is given in the Appendix.

Our approach was different, since our estimate of the Jovian background was obtained using a linear fitting. The band structures in Jupiter's atmosphere are not perfectly uniform, and the fit cannot capture all spatial variations. The formula used by Sparks et al. (2016) cannot, therefore, be directly used in our case, as the discrepancy between observation and model adds an additional uncertainty. Instead, a similar relationship between σ and $\langle I_0 \rangle_{5\times5}$ was obtained directly from each observation. First, $I_{\text{obs}}/I_0 - 1$ was computed in the full 35 km resolution frame. A moving 5×5 pixels standard deviation filter was then applied, effectively calculating the variation of the z statistic in each pixel of the 5×5 moving average frame. The relationship $\sigma_{5\times5} = \sqrt{1/(a \times \langle I_0 \rangle_{5\times5} + b)}$ was fitted between the pixels from the background region (inside an annulus from 2 to 4 Europa radii) and the pixels strictly inside the disk, as shown in Figure 2. This way, pixels from the limb region are not used for the fitting, yet the obtained relationship should represent both the background and the on-disk models and therefore can be applied to the limb

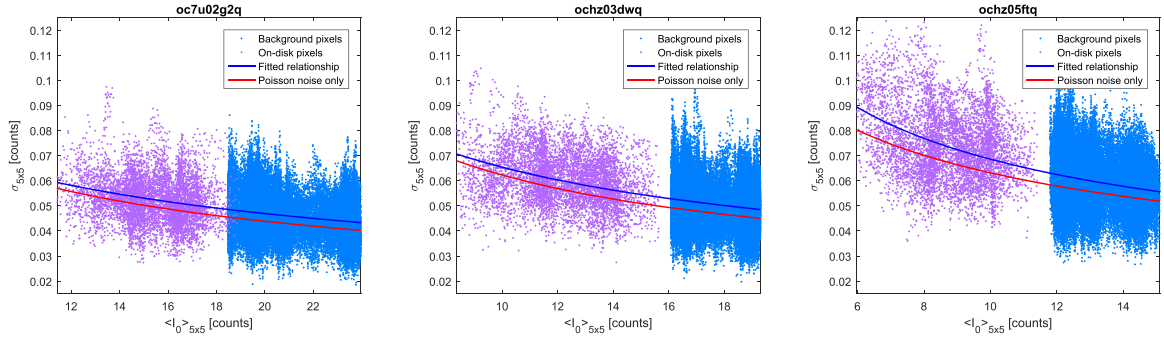

Figure 2. Relationship between the model counts $\langle I_0 \rangle_{5\times5}$ and the variation of the z statistic inside each 5×5 averaged pixel $\sigma_{5\times5}$ for oc7u02g2q (left), ochz03dwq (middle), and ochz05ftq (right). Light blue dots are pixels from the background, which have a higher count rate compared to the pixels from the disk, shown in purple. The relationship is fitted by the blue solid line, compared to the Poisson noise–only relationship, shown by the red solid line.

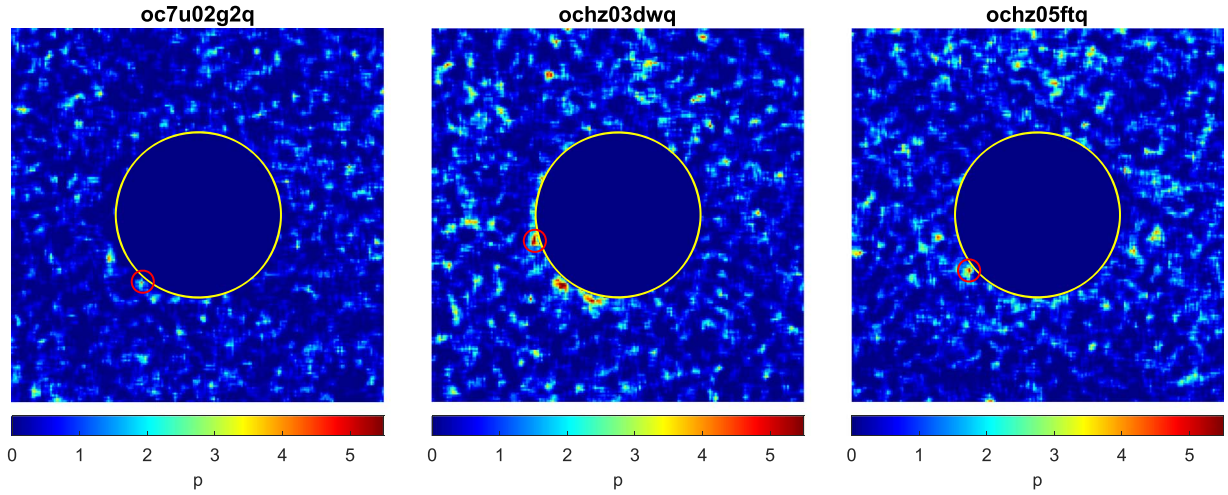

Figure 3. The $p$statistic obtained for oc7u02g2q (left), ochz03dwq (middle), and ochz05ftq (right).

region, which is affected by both the background and the disk models.

The histograms of the residual (i.e., observation $\sigma_{5\times5}$ minus the fitting) were investigated to see whether they follow a normal distribution centered around zero, indicating that the fitted expression is an acceptable estimate of the noise. However, the observed $\sigma_{5\times5}$ is consistently larger than the expectation from pure Poisson noise (computed using an artificial observation, created by adding randomly generated Poisson noise to the model), as shown by the red solid line in Figure 2. As previously mentioned, this larger variance can be attributed to the local mismatch between the observation and the model, adding to the observation Poisson noise. This can also be seen in the width of the $\sigma_{5\times5}$ residual from the fitting (calculated taking the standard deviation after removing the fitted relationship) that are 22%, 23%, and 24% larger than for a residual from pure Poisson noise for oc7u02g2q, ochz03dwq, and ochz05ftq, respectively. Note that the slightly different values between the three observations are due to the different mean count rate of each observation. The fitted relationship for $\sigma_{5\times5}$ was used to normalize the z statistic based on the model counts for each of the 5×5 averaged pixels.

Finally, for the purpose of comparison, the p statistic was obtained as $p = -\log((1 - \mathrm{erf}(-z/\sqrt{2}))/2)$, where erf is the error function. The p statistic is related to the likelihood of an event with significance z to occur randomly, assuming z follows a normal distribution. Figure 3 shows the resulting p-statistic results for the three observations, which are comparable to Figures 6, 7, and 9 from Sparks et al. (2016). Differences in the noise pattern can be attributed to the slight differences in the image reconstruction process, e.g., mapping to the 35 km frame, as well as differences in how the Jovian background was obtained. One plume candidate can be identified in each of the three observations and is indicated by the red circle in Figure 3. These plume candidates are the same as discussed by Sparks et al. (2016), for which the z-statistic results were 3.9σ, 4.4σ, and 4.5σ for oc7u02g2q, ochz03dwq, and ochz05ftq, respectively, compared to 3.8σ, 4.6σ, and 4.3σ derived presently for the corresponding observations. These values describe the highest negative outlier pixel (5×5 moving average) of the z statistics around the plume location and are summarized in Table 1. Note that some outliers also with significance around 4.5σ can be seen in the southwest limb of the ochz03dwq observation. These can be seen in the results from Sparks et al. (2016) too, but with lower significance, and they were not quantitatively analyzed as plume candidates. For the purpose of comparison, these are not discussed here either, but nonetheless, it is important to acknowledge that these pixels would also be relevant in terms of their likelihood to occur randomly.

The z statistic is used in the rest of the paper to discuss the plume significance, since it is, by construction, in units of σ, making it more intuitive to use compared to the p statistic. Moreover, since plumes are seen as negative outliers in the z statistics but their significance is usually discussed in terms of positive σ, $-z$ will be used instead of z for the sake of

Table 1
$-z$Statistic for the Negative (Plume Candidates) and Positive Limb Outliers of Each Observation

	Observation	Sparks et al. (2016)	Reproduction	Position Adjustment	σ_z Correction
Negative outlier	oc7u02g2q	3.9σ	3.8σ	4.3σ	$3.3^{+0.4}_{-0.5}\sigma$
	ochz03dwq	4.4σ	4.6σ	3.4σ	$2.8^{+0.1}_{-0.4}\sigma$
	ochz05ftq	4.5σ	4.3σ	3.9σ	$3.3^{+0.1}_{-0.5}\sigma$
Positive outlier	oc7u02g2q	N/A	-5.4σ	-4.2σ	$-3.2^{+0.4}_{-0.4}\sigma$
	ochz03dwq	N/A	-4.0σ	-3.6σ	$-3.0^{+0.5}_{-0.1}\sigma$
	ochz05ftq	N/A	-3.3σ	-2.9σ	$-2.5^{+0.4}_{-0.0}\sigma$

convenience, as shown in the top row of Figure 4. The $-z$ statistic also gives a similar visual comparison to the p statistic shown by Sparks et al. (2016).

2.4. Positive Outliers

Section 2.3 only discussed the significance of negative z outliers. However, looking at outliers in the positive side of the z statistic is also important. The underlying assumption of the analysis by Sparks et al. (2016) was that—apart from the negative outliers from plume absorption—there are no other sources or sinks of emission around the limb of Europa.

The bottom row of Figure 4 also displays the positive side of the z statistic (here shown in the negative side, as $-z$ is displayed). The location of the positive outlier with the largest significance is shown in each observation by the orange circle. The significance of these outliers is reported in Table 1, and one can see that outliers with large significance are also found around the limb. In particular, in the case of oc7u02g2q, the significance of the positive outlier is much larger than the negative outlier that has been attributed to plume absorption.

Positive outliers are omitted in the analysis by Sparks et al. (2016) and not considered or interpreted. To our knowledge, there is no reasonable physical explanation for the positive outliers that are yet present. Auroral FUV emissions at Europa are too weak (Roth et al. 2016) to affect the broadband FUV images. Hence, positive outliers at the limb should not be physically present in the data and seriously question the use of negative outliers as diagnostic for absorption by plumes. We therefore further investigated the systematics and uncertainties of the z statistic used for the analysis.

3. Investigation of Systematic Uncertainty Sources

3.1. Location of Europa

As previously mentioned, the exact location of Europa's center in the *HST* frame is unknown. Instead, the position has to be determined using the image itself, introducing an uncertainty to the analysis. Applying an automatic detection method on Europa's disk, such as Hough transforms (Duda & Hart 1992), is challenging, since the surface reflectance largely varies between the leading and trailing hemispheres, thus introducing error in the location of the center. Adjusting the position manually was not considered an acceptable method either. We therefore developed a custom method to minimize the misalignment between the observation of Europa and its model.

Angular bins were fixed above the limb of the model, as shown in the left panel of Figure 5. The angular separation of the bins is 5°, and they extend up to 5 pixels radially above the limb. The position of these angular bins is fixed in the model frame, as the angular diameter of Europa in the 35 km frame is well known, and the center of the model disk is located at the center of the frame by design.

The metric ϵ is introduced to quantify the agreement between a model image M (Equation (4)) and an observation (or an artificially generated noise image based on the model) and is defined as the standard deviation of the limb angular profile obtained by subtracting the observation from the model. This is calculated by first taking the mean of the difference between observation and model in each angular bin, thus creating a profile of the difference as a function of the angular bins around the disk. Then, ϵ is computed by taking the standard deviation of this angular profile. The minimum of ϵ suggests that the disks in both the observation and the model are in best agreement, whereas a larger result indicates a misalignment. Intuitively, this can be understood as having on-disk features of the misaligned observation frame bleeding into the angular bins fixed in the model frame, thus increasing the variance of the angular residual profile, which is measured by ϵ. Note that this method requires the Europa disk to have enough contrast with respect to Jupiter's background in order to be valid. This is the case for the three observations considered, where the Europa disk has lower photon counts than the background. It also requires that the number of off-disk features (e.g., plumes) that significantly affect the observation is small.

The validity of the method was tested using artificial observations created by adding Poisson noise to the model. Multiple independent trials ($N = 10^4$) were performed. For each trial, randomly generated Poisson noise was added to the model to create the artificial observation, which was then shifted from the perfectly centered position to one of the eight neighboring pixels (i.e., four 1 pixel shifts in the horizontal and vertical directions and four $\sqrt{2}$ pixel shifts in the diagonal directions). The method was applied for each of the shifted artificial observations, as well as the centered case: the difference between artificial observation and model was computed before averaging the residual in each of the angular bins, and finally, the standard deviation of the obtained average angular residual profile was calculated. The right panel of Figure 5 shows an example of three average angular residual profiles for the centered case, a 1 pixel shift to the north, and a $\sqrt{2}$ pixel shift to the northeast. These are the average profiles of the N trials, but single profiles can vary, largely due to the randomness of the Poisson noise introduced, which is shown by the shaded area corresponding to the $\pm 1\sigma$ spread. One can see that these regions overlap, meaning there is a chance ϵ might not always be minimal at the centered position. Out of the N trials performed, the centered position was correctly determined compared to a 1 pixel shift in 83% of the cases and a $\sqrt{2}$ pixel shift in 97% of the cases. This provided confidence in the reliability of the method to correctly find the best

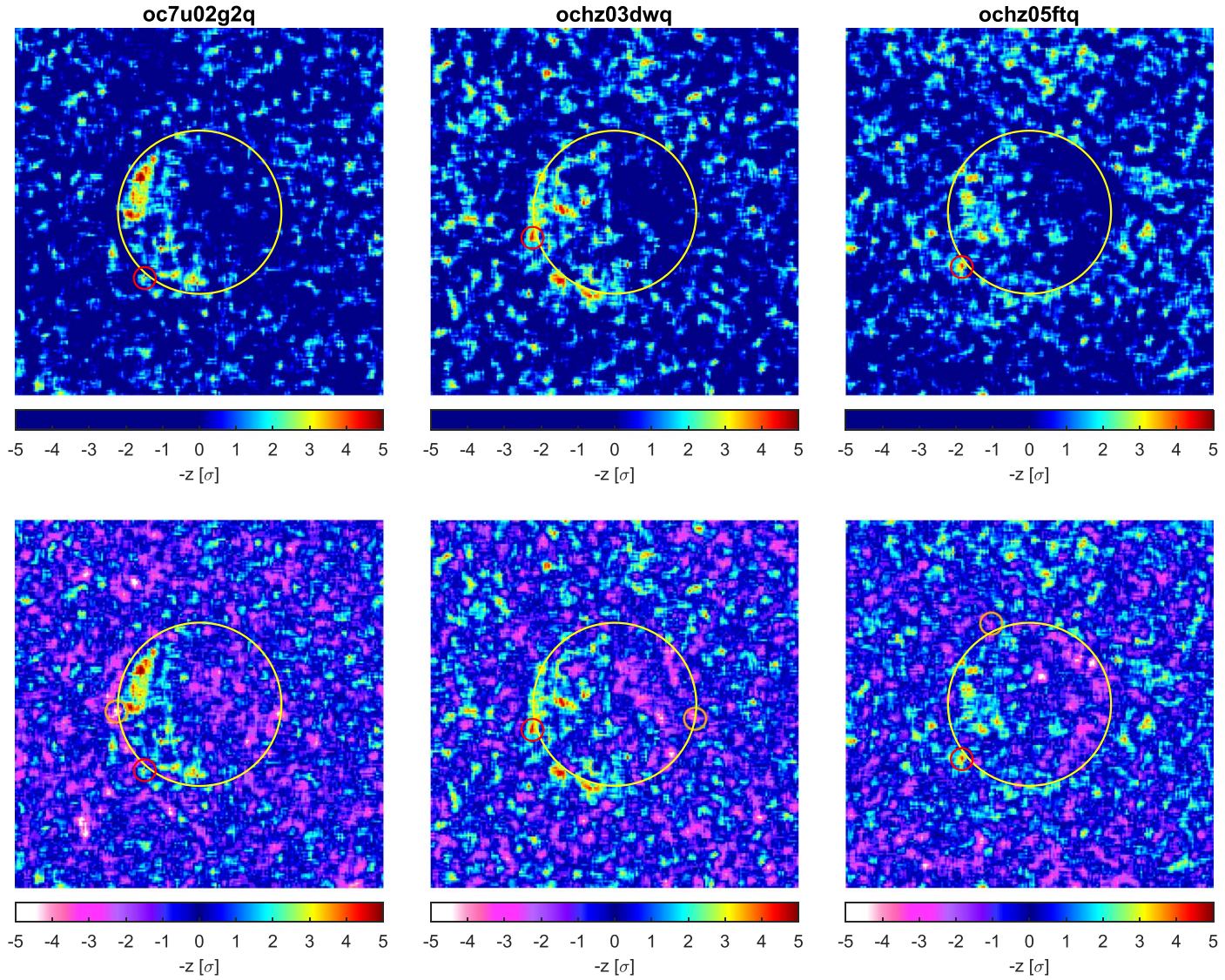

Figure 4. The top row shows the one-sided display of the $-z$ statistic obtained for oc7u02g2q (left), ochz03dwq (middle), and ochz05ftq (right) as a comparison to the p statistic shown in Figure 3. Positive z are not shown here, and yellow indicates negative outliers with 3σ significance. The bottom row shows the full display of the $-z$ statistic obtained for oc7u02g2q (left), ochz03dwq (middle), and ochz05ftq (right). For each image, one negative outlier around the limb is shown by the red circle and one positive outlier by the orange circle. Yellow and pink, respectively, indicate negative and positive outliers with 3σ significance.

coalignment between the observation and the model, at least within a 1 pixel accuracy.

The method was then applied to the *HST* observations: each of the three observation frames was shifted in both the vertical and horizontal directions with respect to their respective model frame, and ϵ was calculated for each of the shift combinations. Figure 6 shows a map of ϵ as a function of the vertical and horizontal shift of the observation frame with respect to the model frame. Note that the center (i.e., no shift) is defined as the location that yielded the best agreement with the reproduction of Sparks et al. (2016; displayed in Figure 3). The best alignment according to our method differs from these positions by at least 1 pixel.

A simple analysis was then conducted to determine the effect of such misalignments on the resulting z statistic. Similarly as performed earlier, artificial observations were created by adding Poisson noise to the model for $N = 10^4$ independent trials. In each trial, the z statistic was computed for six cases: a centered case with no shift between the artificial observation and the model and five cases of possible shifts: north, south, east, west, and northeast. Shifts to the west, northeast, and north, respectively, correspond to the derived shift for ochz05ftq, ochz03dwq, and oc7u02g2q. In each case and for each trial, the z statistic of the pixels in each of the angular bins was stored, resulting in a histogram of the z statistic for each angular bin. Figure 7 shows the resulting histogram distribution of the z statistic as a function of angle for each case.

The assumption taken by Sparks et al. (2016) is that the z-statistic mean is zero, which is indeed the case for the centered case. However, this assumption is no longer valid in the case of a misalignment between the observation and the model. A misalignment offsets the mean of the z statistic: for example, in the case of a 1 pixel horizontal shift (middle right panel of Figure 7), one can see the effect of the darker trailing hemisphere bleeding outside the west limb (i.e., 180°) and making the mean of the z statistic shift by about -1σ.

Another important result becomes evident in these histograms of Figure 7: the limb region of the trailing hemisphere

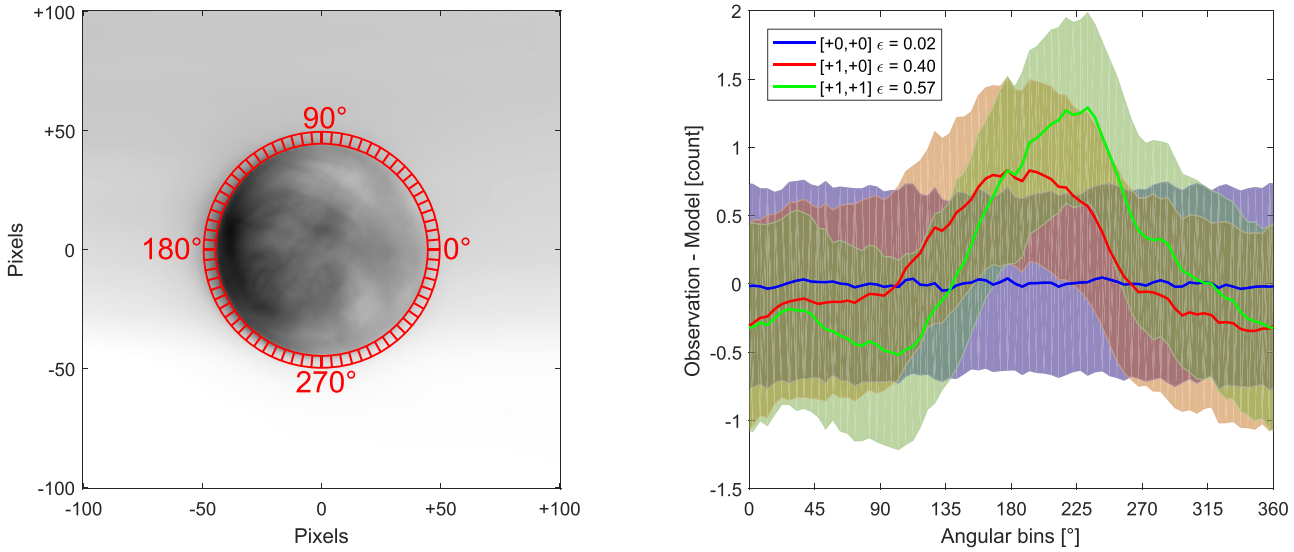

Figure 5. Left: angular bins outside the limb in the reference frame of the model. The angular step of each bin is 5°, while the radial distance is up to 5 pixels above the limb. Right: example of the angular residual profile for three shifts of the artificial observation: centered ([+0, +0]), 1 pixel horizontally toward the east ([+1, +0]), and 1 pixel horizontally and vertically toward the northeast ([+1, +1]). The solid lines show the average residual, whereas the shaded regions indicate the 1σ spread from the mean due to the Poisson noise. The metric ϵ is computed as the standard deviation of the average profiles (solid lines).

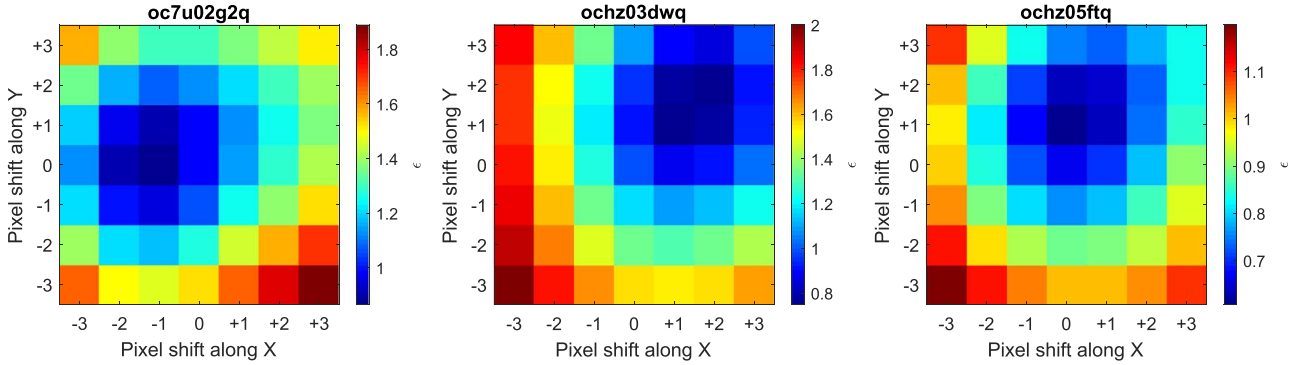

Figure 6. Assessment of the disk position by comparing observation and model: ϵ as a function of the vertical and horizontal shifts of the observation frame with respect to the model frame for oc7u02g2q (left), ochz03dwq (middle), and ochz05ftq (right). The center ([0, 0]) pixel relates to the assumed center from Section 2. The minimum value indicates the best-fit position.

(between angles 90° and 270°) is more affected by a shift of the location than the leading hemisphere, independent of the direction of the shift. Both the shift to the east and the shift to the west offset the mean z statistic in the trailing hemisphere (near 180°) by up to $\pm 0.9\sigma$, compared to only $\pm 0.3\sigma$ in the leading hemisphere (near 0°). Similarly, for the north and south shifts, the deviations of the mean z statistic are clearly stronger above the trailing hemisphere (between 90° and 270°), even though the mean z (black line) is crossing the zero line near 180°. The reason for this leading–trailing asymmetry is the larger gradient in the signal between the generally brighter background and the darker trailing hemisphere compared to the less dark (and thus more similar to the background) leading hemisphere. Due to this, statistical outliers with particularly high levels of apparent significance are more likely to happen around the limb of the trailing hemisphere in case of any misalignment of Europa in the model with respect to the real location (either in the positive or negative side of the z statistic, depending on the misalignment direction).

This illustrates the importance of precisely determining the position of Europa in the observation frame when discussing plume candidates, as misalignments with the model distort the statistics. According to our method, the location of Europa we assumed to reproduce the results from Sparks et al. (2016) is off from the best-fit location by at least 1 pixel in all three images.

The z statistic was recalculated by adjusting the position of the Europa observation with respect to the model based on Figure 6 and is shown in Figure 8. A different significance for the plume candidate is derived as a result of the positional adjustment, with a $-z$ statistic of 4.3σ, 3.4σ, and 3.9σ compared to the previous 3.8σ, 4.6σ, and 4.3σ obtained when reproducing the Sparks et al. (2016) results, as reported in Table 1. Note that the significance decreased in case of ochz03dwq and ochz05ftq but increased for oc7u02g2q due to the direction of the misalignment. Similarly, the significance of the positive outliers is changed from -5.4σ, -4.0σ, and -3.3σ previously to -4.2σ, -3.6σ, and -2.9σ after adjusting the position, respectively.

3.2. *Unnormalized Background, On-disk, and Limb Statistical Distributions*

A closer look at the distribution of the z statistic is needed in order to properly discuss the results and derive quantitative

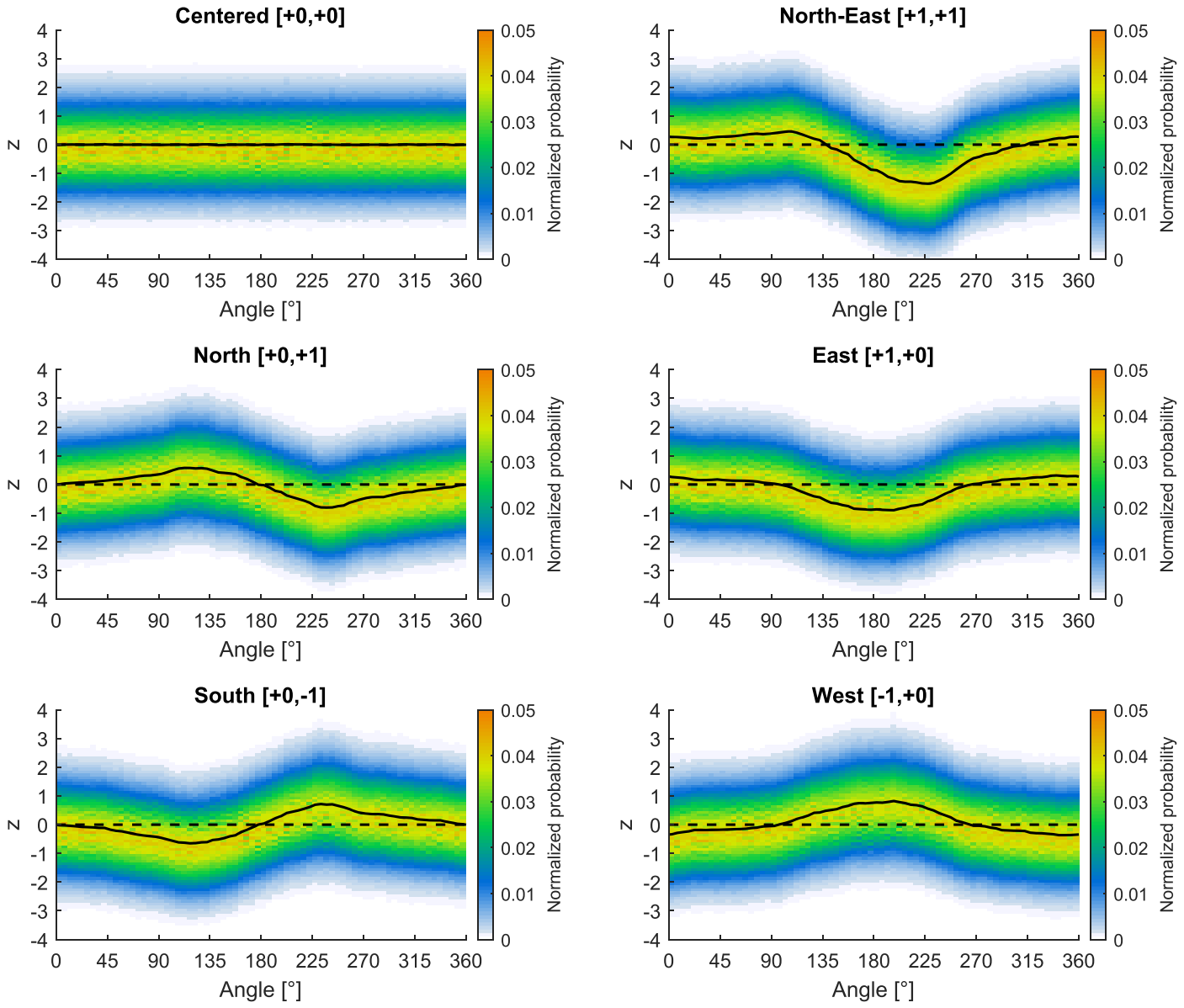

Figure 7. The z-statistic distribution around the limb for six different assumed disk positions from the sample of 10^4 trials: no shift between artificial image and model (top left panel), shift of the artificial image to the northeast with respect to the model ([+1, +1], top right panel, similar to ochz03dwq), shift to the north ([+0, +1], middle left panel, similar to ochz05ftq), shift to the east ([+1, +0], middle right panel), shift to the south ([+0, −1], bottom left panel), and shift to the west ([−1, +0], bottom right panel, similar to oc7u02g2q). The x-axis uses the coordinate system shown in Figure 5, where 0° is the right/leading hemisphere, 90° is toward north, and 180° is the left/trailing hemisphere. The area under the z statistic for each angular bin is normalized to unity. The black solid line shows the average of the z-statistic distribution.

conclusions. Figure 9 shows the histograms of the z statistic for the background (pixels inside an annulus region between 2 and 4 Europa radii), disk (region inside the Europa radius), and limb (pixels in a disk region between the limb and 5 pixels above the limb) for each of the three observations. One can see that the variance of the z statistic, represented by σ_z, is significantly larger than unity both in the background and on-disk, indicating that the z statistic is not properly normalized in both cases. This can be related to a spatial mismatch between the observation and the model: although both the background and on-disk models compare adequately to the observation on a global (i.e., statistical) scale, as was shown by the $\sigma_{5\times5}$ relationship from Section 2.3, both models do not represent the observation accurately for small spatial features, which leads to an improperly normalized z with $\sigma_z > 1$. This is also directly linked to the larger width of the residual from the fitting discussed in Section 2.3 and shown in Figure 2, which was about 22%–24% larger than the purely Poisson noise case and is comparable to the σ_z observed in Figure 9. This additional uncertainty is due to the discrepancies of the model to the observation on small spatial scales that cannot be normalized away by $\sigma_{5\times5}$, thus remaining in the resulting z statistic.

The bottom row of Figure 9 shows that σ_z in the limb region is also larger than unity, with values larger than the background σ_z (16%–17% larger than unity) but smaller than the on-disk σ_z (37%–51% larger than unity). Based on the N trials simulation, the limb σ_z is expected to be around unity, with an uncertainty (1σ width) of 0.06. The larger σ_z observed around the limb is therefore also due to a discrepancy between the model and the observation.

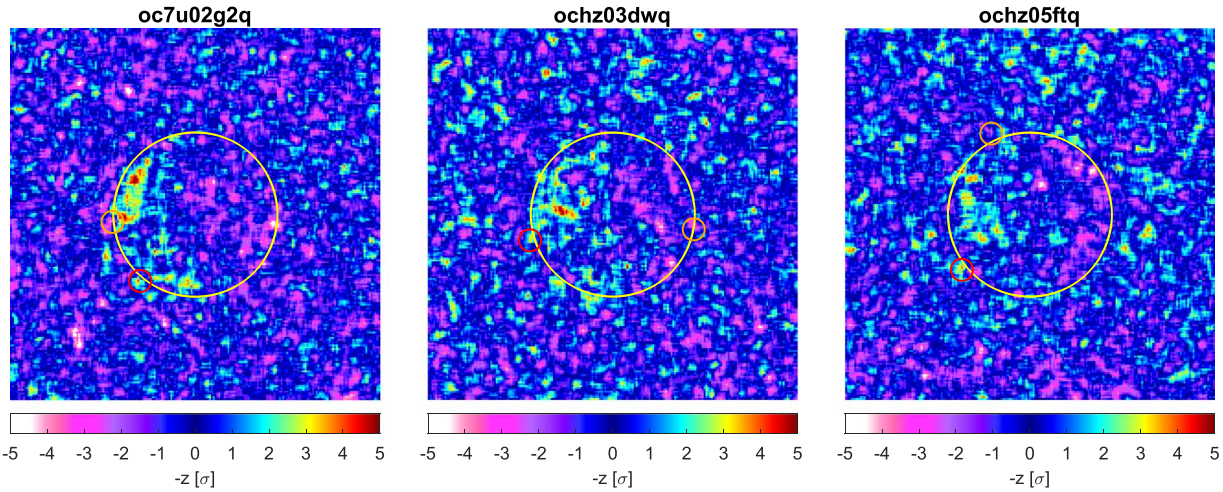

Figure 8. Full display of the $-z$ statistic obtained at the best alignment between observation and model for oc7u02g2q (left), ochz03dwq (middle), and ochz05ftq (right). Yellow and pink respectively indicate negative and positive outliers with 3σ significance.

This is further confirmed by using a Shapiro–Wilk test of normality on the z statistics (Shapiro & Wilk 1965). A resulting p-value lower than a given significance level (typically 0.05) indicates that the tested values were not drawn from a normal distribution, while a p-value larger than the significance level suggest that the distribution might be normally distributed. Applying this test to a randomly selected sample of z-statistic pixels in the Jovian background, on Europa's disk, and at the limb gives variable results: for oc7u02g2q, a p-value of 0.0105 was found for the background, 0.0002 for the disk, and 0.3964 for the limb samples. This would indicate that the z statistic both in the Jovian background and on the disk is not normally distributed. Note that the p-value larger than 0.05 for the limb sample does not strictly confirm the normality of the distribution, and this result could be due to the sample size. In the case of ochz03dwq, p-values were 0.5324, 0.0546, and 0.0021, respectively, which in this case clearly rejects the normal hypothesis for the z statistic at the limb. Results for ochz05ftq were similar to oc7u02g2q, with p-values 0.0056, 0.0049, and 0.1259, respectively. Overall, the Shapiro–Wilk test seems to indicate that the assumption of normality for the image statistics near the limb (Sparks et al. 2016) is not generally valid, which also invalidates the σ significance of any results drawn from it.

Although a proper correction of the results is not possible because the distribution of the z statistic for each pixel is unknown, Figure 9 still provides an estimate of how much the width of the distribution was affected. Dividing the significance of each plume by the σ_z of the limb distribution gives an estimate of the true significance of the plume, while dividing by the background σ_z provides an upper limit. Similarly, dividing by the σ_z of the disk provides a lower limit. Applying the correction, the resulting $-z$ statistics of each of the three plume candidates are $3.3^{+0.4}_{-0.5}\sigma$, $2.8^{+0.1}_{-0.4}\sigma$, and $3.3^{+0.1}_{-0.5}\sigma$.

It is important to notice that this affected the results from Sparks et al. (2016) too. Even though their normalization of the z statistic works in the background, because it was derived from the observation itself, the z statistic at the limb and on-disk would not be properly normalized, since the on-disk model does not perfectly match the observation. This can be seen in the on-disk residual in the left part of Figures 6, 7, and 9 from their article.

Note that the limb distributions of the z statistic are also slightly offset from zero, by $+0.45\sigma$, -0.25σ, and -0.35σ, respectively, for oc7u02g2q, ochz03dwq, and ochz05ftq. The σ_z correction should also be applied to this offset, reducing it to, respectively, $+0.35^{+0.03}_{-0.05}\sigma$, $-0.20^{+0.03}_{-0.02}\sigma$, and $-0.30^{+0.04}_{-0.00}\sigma$. The N trials run with purely Poisson noise artificial observations from Section 3.1 indicated that the 1σ uncertainty around zero of the z-statistic distribution mean for a perfectly aligned case (i.e., [0, 0] shift) is 0.11. The observed offsets of the limb distribution are slightly larger than that, suggesting that some residual misalignment between observation and model might remain. However, since the ϵ method was considered as a reference for the alignment, the limb distribution was not corrected by its observed offset from zero.

The significance of the positive outliers around the limb is also affected by the positional adjustment of the image and the σ_z correction. The resulting $-z$ statistic for each of the highest positive outliers in each of the three observations is, respectively, $-3.2^{+0.4}_{-0.4}\sigma$, $-3.0^{+0.5}_{-0.1}\sigma$, and $-2.5^{+0.4}_{-0.0}\sigma$. Table 1 gives a comparison between the largest corrected negative (i.e., plume candidate) and positive outliers for each observation.

4. Statistical Significance of the Limb Minima and Maxima

The likelihood of such plume candidate results occurring randomly around the limb can be estimated by considering the number of pixels in the region. In the 35 km frame, a disk extending from the limb to 5 pixels above the limb contains about 1500 pixels. In such a sample size, at least one negative and one positive outlier with σ equal to -3.2 and 3.2, respectively, are expected from a purely random Poisson (or Gaussian) distribution. This is also true in the 5×5 moving average frame, even though each 5×5 averaged pixel is no longer statistically independent, because the z statistic is normalized in the 5×5 frame. One can see that the largest obtained plume significance after correction using the width of the limb distribution of 3.3σ is therefore expected in almost every image (technically, in 1.4 images). In addition, outliers with lower/larger significance could also occur: a 3.7σ outlier (plume significance when corrected by the width of the background distribution) is expected in one out of six images, which is exactly the duty cycle of 17% stated by Sparks et al.

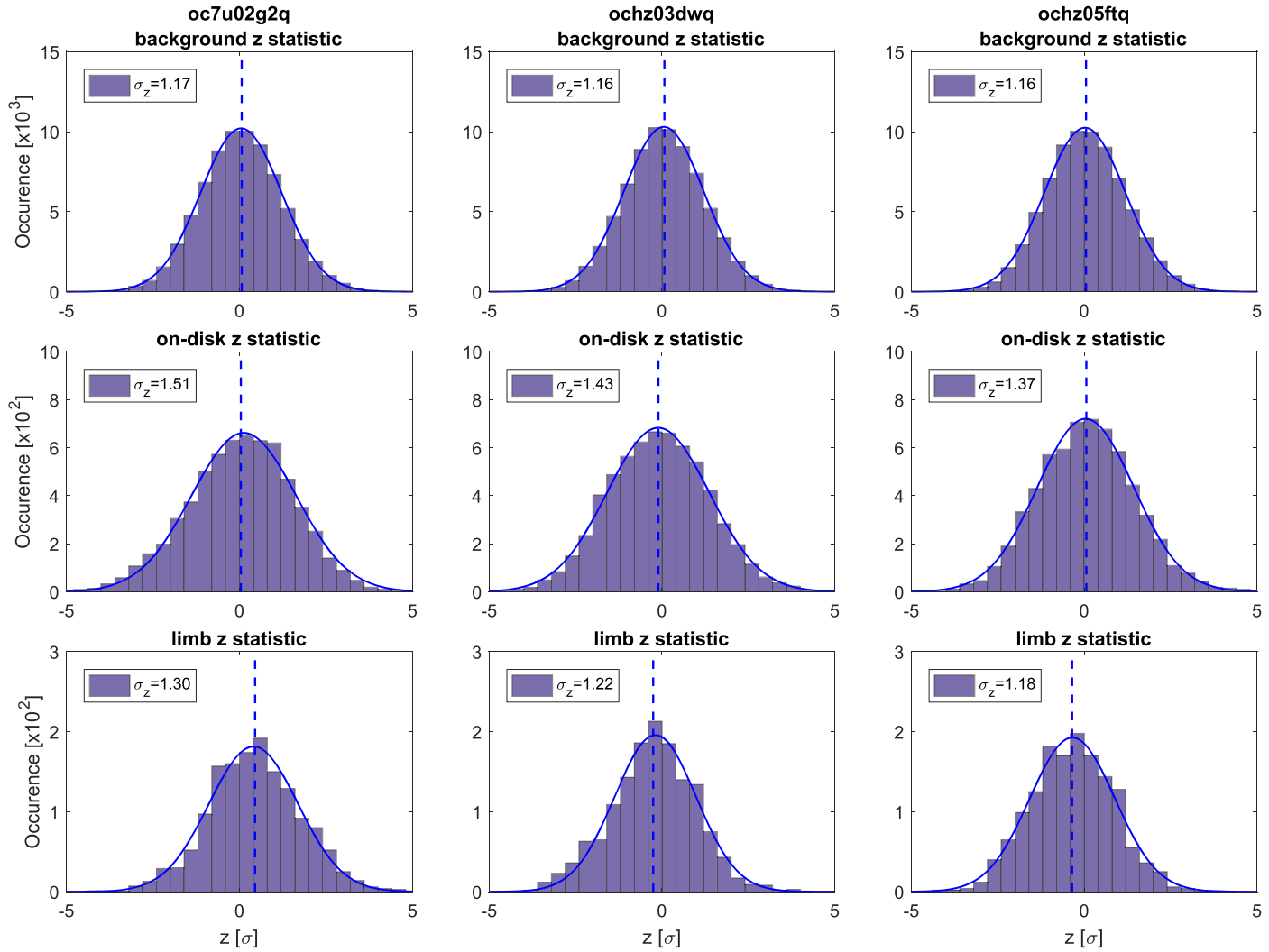

Figure 9. Histograms of the z statistic for oc7u02g2q (left), ochz03dwq (middle), and ochz05ftq (right). The top row shows results for the background region, the middle row for the disk region, and the bottom row for the limb region. Dashed lines show the average z statistic, and solid lines show a Gaussian fitting with the width σ_z given in the legend.

(2017). A 4.0σ outlier is expected around the limb in one out of 22 images.

Figure 10 illustrates the visual appearance of a purely statistical outlier and the differences for different misalignments of the model. The artificial observation (model with added Poisson noise) used in Figure 10 was taken from one of the N trials from Section 3.1, and contains a negative outlier at the limb with significance above 3.2σ. We deliberately selected a case where this outlier is located in the lower left limb to demonstrate the effect of misalignment in this region between the observation and the model; the significance of the outlier in the $-z$ statistic increases from 3.8σ in a perfectly aligned case, to 4.6σ in the case of a 1 pixel shift of the observation toward the east, to 5.4σ in the case of a 1 pixel shift toward both the north and the east. The increase in significance is consistent with the average offset of the z statistics near an angle of 225° due to misalignment, as shown in Figure 7.

Note that a negative outlier seen at the same location on multiple observations—as inferred in Sparks et al. (2017) for one of the multiple plumes derived in the three images from Sparks et al. (2016)—generally increases the combined significance of that outlier. If one -3.2σ outlier is expected somewhere outside the limb in each observation, the chances of randomly detecting a similar outlier in the same 5° angular segment (roughly representing the width of a feature; see left panel of Figure 5) is $1/72$, or about 1.4%. Given that plume outliers were already detected in at least three different limb locations in Sparks et al. (2016), the chance of a redetection through a purely statistical outlier in one of the three locations is $3/72$, or 4.2%. In addition, it is important to also remember that the z statistic in the trailing hemisphere is more likely to be skewed by misalignment between observation and model compared to the leading hemisphere, as shown in Figure 7, which could lead to more outliers observed in the same location of the trailing hemisphere. To accurately assess the combined significance of a detection of the same feature in two images, a separate, quantitative analysis is required. In this paper, we focus only on the first three plume detection transit images.

For these three images, we conclude that the obtained maximum and minimum z-statistic limb pixel values are consistent with and can be explained by pure statistical fluctuations of the measurements.

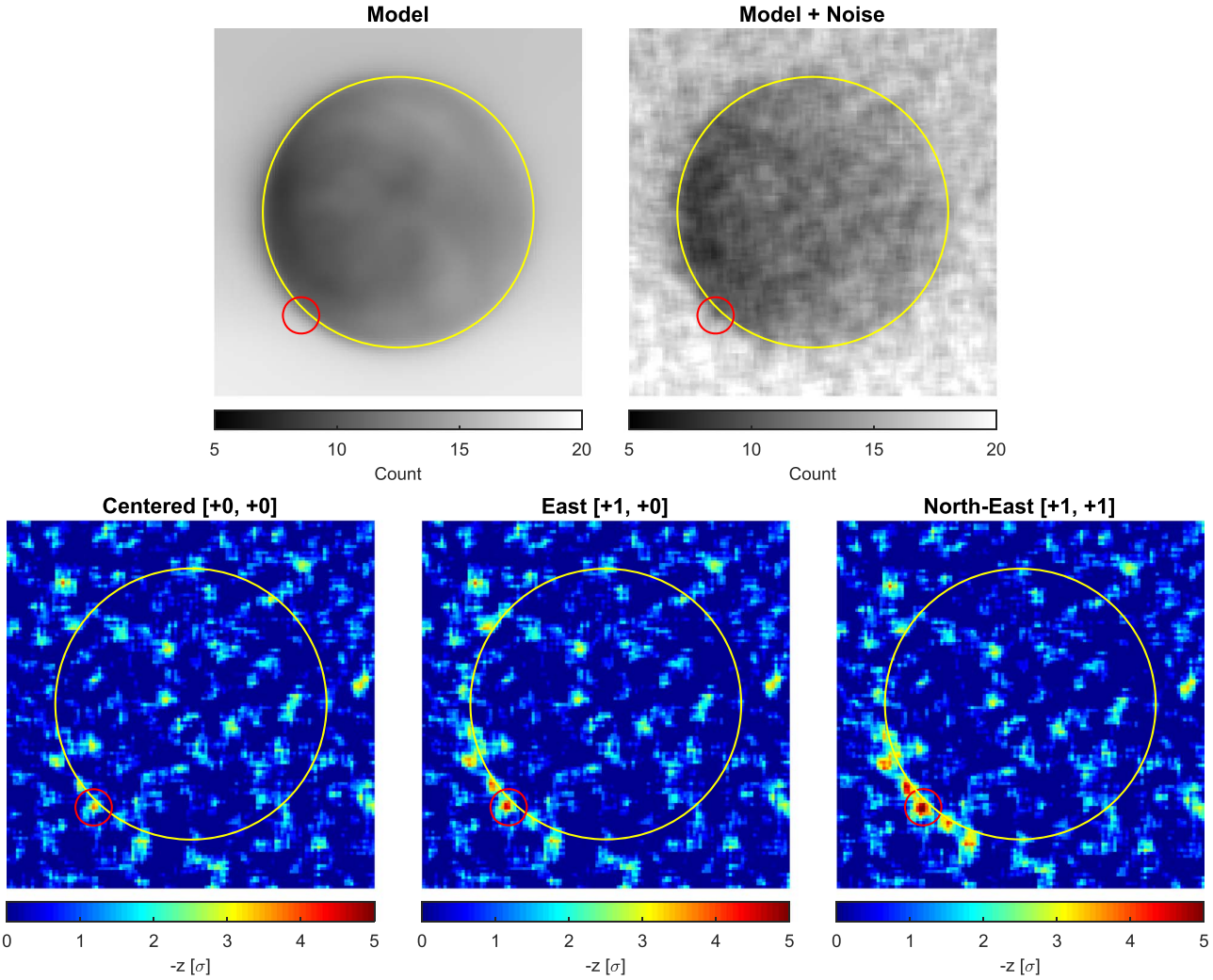

Figure 10. Example of a purely statistical negative outlier seen in artificial data. The top row shows the model on the left (based on the ochz03dwq observation) and the artificial observation (model + Poisson noise) on the right. The bottom row shows the one-sided $-z$ statistic for three cases: no shift between the artificial observation and model (left), shift of the observation to the east with respect to the model ([+1, +0]; middle panel) and to the northeast ([+1, +1]; right panel). The red circle shows the location of the negative outliers, with $-z$ statistic values of 3.8σ, 4.6σ, and 5.4σ, respectively, for the three cases.

5. Summary and Conclusion

The possible presence of water plumes emanating through cracks in Europa's icy surface is important for future scientific exploration, as the prospect of probing the Europa inner ocean for signs of organic molecules from space could lead to major scientific discoveries. Several authors reported evidence of water plumes in recent years, and confirming these results by independent analysis of the data is therefore of prime importance. The observations from Sparks et al. (2016) were reanalyzed herein. Using their method, a similar significance level for the negative outliers was obtained. However, positive outliers with large significance were also observed around the limb. Hence, an in-depth analysis of the systematic sources of uncertainty was conducted to better understand the statistical results.

First, we observed that misalignment between the observation frame and the model frame used to compute the z statistic can offset the mean of the z-statistic distribution from zero (note that this would also apply if an average of multiple observations is used as the model frame). The location of Europa in the *HST* frame is unknown due to the uncertainty in the absolute pointing of the telescope in this observation mode and difficult to estimate given the observation noise. A deterministic method was developed to coalign observation and model by minimizing the residual variance of their difference in angular bins located above the limb. This metric, called ϵ, is the minimum in a perfectly coaligned case and was shown to correctly find a 1 pixel misalignment in 83% of cases. Using this method, the disk positions, for which the results from Sparks et al. (2016) were best reproduced, differ from our best-fit location by at least 1 pixel in all three images. We also investigated how the z statistic around the limb was distorted by misalignment. This revealed that the offset from zero in the z-statistic mean was three times larger above the darker trailing hemisphere compared to the brighter leading hemisphere. In other words, false detections (both maximum and minimum) due to misalignment are more likely in the trailing hemisphere, where most of putative plume features in the transit images are found.

The distribution of the z statistic in the background, on-disk, and around the limb was shown to have a width σ_z larger than unity even after correcting for location misalignment. This can be explained by the fact that the model does not perfectly match the observation and introduces an additional uncertainty

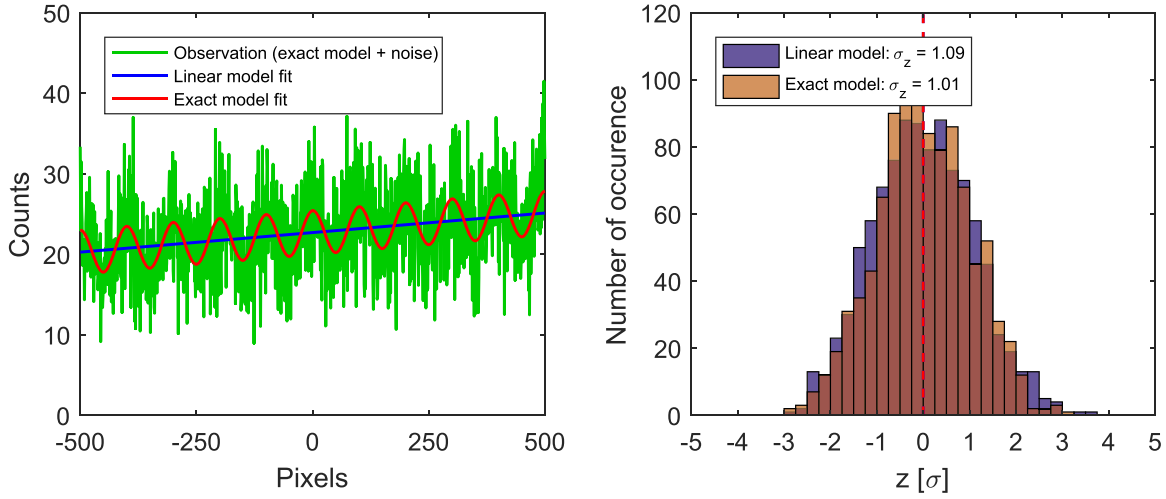

Figure 11. Left: simulated signal (exact model + Gaussian noise; green line) with the linear (blue line) and exact (red line) model fits. Right: histogram of the z statistic for the linear (blue) and exact (red) models, where the σ_z is given for each in the legend.

on the z statistic that cannot be removed by normalization. The distribution of the z statistic around the limb was also shown to remain slightly offset from zero, which might be due to possible residual misalignment of the observation to the model. Correcting for σ_z is required in order to properly normalize the z statistic in units of σ and assess the significance level. In our case, both the background σ_z and the on-disk σ_z were used to provide an upper and lower limit for the correction, respectively. Note that this should also be applied in the case of Sparks et al. (2016), since their on-disk σ_z should also be larger than unity, therefore making the limb σ_z larger than unity too. The σ_z of the limb distribution was observed to be in between the ones from the background and the on-disk distributions, which is expected due to the PSF smearing, making both models merge at the limb. Table 1 summarizes the results when accounting for these corrections in the analysis. Depending on the observation, the significance of the plume candidate decreased by 0.5σ–1.8σ compared to the reproduction of the Sparks et al. (2016) results.

We furthermore found that the decreased significance of the plume-related outliers is consistent with purely statistical fluctuations in an ensemble size equal to the number of pixels in the limb region. This means that the negative outliers do not necessarily require a systematic (physical) deviation in the source. The measured positive outliers (for which a physical explanation is lacking) have a similar significance as the negative outliers in all three images after our corrections, and they are thus similarly consistent with the expected statistical fluctuations.

In conclusion, an unambiguous detection of negative limb anomalies, as generated by local plumes, in the three *HST*/STIS transit images is severely hampered by the technical complexity of the observation and the relatively low signal. We find that the resulting significance of putative plume regions in all three analyzed images is marginal when correctly accounting for the statistical fluctuations and applying a deterministic method to locate Europa's position. The negative outliers present in the three images hence do not provide evidence for local absorption by plumes.

L.R. and G.G. appreciate the support from the Swedish Research Council (grant 2017-04897) and the Swedish National Space Agency (grant 154/17).

Appendix
Effect of Model Mismatch on the z Statistic

A model incorrectly representing the observation could lead to an improperly normalized z statistic, even if the noise present in the observation is fully known in theory. This is referred to as a mismatch between the model and the observation. For example, in the case of the Jovian background, this could happen if the model used is not able to reproduce the small local variations in the band structure that are buried in the observation noise. A simple example is presented hereafter to illustrate and visualize this effect.

An observed signal is created by adding Gaussian noise to an exact mathematical expression composed of a linear trend (e.g., representing the slow linear trend along Jupiter's band) with a superimposed sine wave with a small amplitude compared to the noise level (e.g., representing local spatial variation along the band structure). This observed signal is then compared to two different models: a linear model only considering the linear trend and the exact model including the superimposed sine wave. In both cases, the z statistic is calculated as $z = (\text{observation}/\text{model} - 1)/\sigma$, with $\sigma = \sqrt{1/\text{model}}$, as is expected for purely Gaussian noise. The left panel of Figure 11 shows the observed signal and the two models. In this example, the average signal count is around 20, resulting in a Gaussian noise σ around 4.5. For comparison, the amplitude of the superimposed sine wave is 3. The right panel of Figure 11 displays the histograms of the z statistics, showing that the width of the distribution σ_z is larger than unity by about 10% in the case of the linear model, and illustrates the effect of model mismatch on the z statistics. Note that, even if providing an exact model, fitting it on a low signal-to-noise ratio observation might still contain significant uncertainty, which might also result in a slightly improperly normalized z statistic.

ORCID iDs

Gabriel Giono https://orcid.org/0000-0001-7925-1555
Lorenz Roth https://orcid.org/0000-0003-0554-4691
Joachim Saur https://orcid.org/0000-0003-1413-1231
Kurt Retherford https://orcid.org/0000-0001-9470-150X

References

Arnold, H., Liuzzo, L., & Simon, S. 2020, JGRA, in press (doi:10.1029/2019JA027346)
Blöcker, A., Saur, J., & Roth, L. 2016, JGRA, 121, 9794
Cook, A. F., Shoemaker, E. M., Smith, B. A., et al. 1981, Sci, 211, 1419
Duda, R. O., & Hart, P. E. 1992, Commun. ACM, 15, 11
Grasset, O., Castillo-Rogez, J., Guillot, T., Fletcher, L. N., & Tosi, F. 2017, SSRv, 212, 835
Greeley, R., Chyba, C. F., Head, I. J. W., et al. 2004, in Jupiter. The Planet, Satellites and Magnetosphere, ed. F. Bagenal, T. E. Dowling, & W. B. McKinnon (Cambridge: Cambridge Univ. Press), 329
Hansen, C. J., Esposito, L., Stewart, A. I. F., et al. 2006, Sci, 311, 1422
Hansen, C. J., Esposito, L. W., & Hendrix, A. R. 2019, Icar, 330, 256
Jia, X., Kivelson, M. G., Khurana, K. K., & Kurth, W. S. 2018, NatAs, 2, 459
Johnson, R. E., Smith, H. T., Tucker, O. J., et al. 2006, ApJL, 644, L137
Khurana, K. K., Kivelson, M. G., Stevenson, D. J., et al. 1998, Natur, 395, 777
Lagg, A., Krupp, N., Woch, J., & Williams, D. J. 2003, GeoRL, 30, 1556
Mauk, B. H., Mitchell, D. G., Krimigis, S. M., Roelof, E. C., & Paranicas, C. P. 2003, Natur, 421, 920
McGrath, M. A., & Sparks, W. B. 2017, RNAAS, 1, 14
Mota, R., Parafita, R., Giuliani, A., et al. 2005, CPL, 416, 152
Oren, M., & Nayar, S. K. 1994, in SIGGRAPH '94: Proceedings of the 21st Annual Conference on Computer Graphics and Interactive Techniques (New York: ACM), 239
Paganini, L., Villanueva, G. L., Roth, L., et al. 2020, NatAs, 4, 266
Pappalardo, R. T., Head, J. W., Greeley, R., et al. 1998, Natur, 391, 365
Phillips, C. B., McEwen, A. S., Hoppa, G. V., et al. 2000, JGR, 105, 22579
Porco, C. C., Helfenstein, P., Thomas, P. C., et al. 2006, Sci, 311, 1393
Proffitt, C., Aloisi, A., Bohlin, R., et al. 2010, STIS Instrument Handbook Version 9.0 (Baltimore, MD: STScI)
Roth, L., Retherford, K. D., Ivchenko, N., et al. 2017, AJ, 153, 67
Roth, L., Retherford, K. D., Saur, J., et al. 2014a, PNAS, 111, E5123
Roth, L., Saur, J., Retherford, K. D., et al. 2014b, Sci, 343, 171
Roth, L., Saur, J., Retherford, K. D., et al. 2016, JGRA, 121, 2143
Saur, J., Feldman, P. D., Roth, L., et al. 2011, ApJ, 738, 153
Schmidt, B. E., Blankenship, D. D., Patterson, G. W., & Schenk, P. M. 2011, Natur, 479, 502
Shapiro, S. S., & Wilk, M. B. 1965, Biometrika, 52, 591
Shemansky, D. E., Matheson, P., Hall, D. T., Hu, H. Y., & Tripp, T. M. 1993, Natur, 363, 329
Silverman, B. 1986, Monographs on Statistics and Applied Probability, Vol. 26 (London: Chapman and Hall)
Smith, H. T., Mitchell, D. G., Johnson, R. E., Mauk, B. H., & Smith, J. E. 2019, ApJ, 871, 69
Smyth, W. H., & Marconi, M. L. 2006, Icar, 181, 510
Spahn, F., Schmidt, J., Albers, N., et al. 2006, Sci, 311, 1416
Sparks, W. B., Hand, K. P., McGrath, M. A., et al. 2016, ApJ, 829, 121
Sparks, W. B., Richter, M., Montiel, E., et al. 2019, ApJL, 871, L5
Sparks, W. B., Schmidt, B. E., McGrath, M. A., et al. 2017, ApJL, 839, L18
Squyres, S. W., Reynolds, R. T., Cassen, P. M., & Peale, S. J. 1983, Natur, 301, 225
Yoshino, K., Esmond, J. R., Parkinson, W. H., Ito, K., & Matsui, T. 1996, CP, 211, 387
Zimmer, C., Khurana, K. K., & Kivelson, M. G. 2000, Icar, 147, 329